An investigation of the thermo-mechanical features of Laohugou Glacier No.12 in Mt. Qilian Shan, western China, using a two-dimensional first-order flowband ice flow model

Yuzhe Wang[1,2], Tong Zhang[3], Jiawen Ren[1], Xiang Qin[1], Yushuo Liu[1], Weijun Sun[4], Jizu Chen[1,2], Minghu Ding[3], Wentao Du[1,2], and Dahe Qin[1]

[1]State Key Laboratory of Cryospheric Science, Northwest Institute of Eco-Environment and Resources, Chinese Academy of Sciences, Lanzhou 730000, China
[2]University of Chinese Academy of Sciences, Beijing 100049, China
[3]Insititute of Polar Meteorology, Chinese Academy of Meteorological Sciences, Beijing 100081, China
[4]College of Geography and Environment, Shandong Normal University, Jinan 250014, China

Correspondence to: Tong Zhang (tzhang@camscma.cn)

Abstract. By combining *in situ* measurements and a two-dimensional thermo-mechanically coupled ice flow model, we investigate the thermo-mechanical features of the largest valley glacier (Laohugou Glacier No.12; LHG12) in Mt. Qilian Shan located in the arid region of western China. Our model results suggest that LHG12, previously considered as fully cold, is probably polythermal, with a lower temperate ice layer overlain by an upper layer of cold ice over a large region of the ablation area. Modeled ice surface velocities match well with the *in situ* observations in the east branch (mainstream) but clearly underestimate the ice surface velocities near the glacier terminus possibly because the convergent flow is ignored and the basal sliding beneath the confluence area is underestimated. The modeled ice temperatures are in very good agreement with the *in situ* measurements from a deep borehole (110 m) in the upper ablation area. The model results are sensitive to surface thermal boundary conditions, for example, surface air temperature and near-surface ice temperature. In this study, we use a Dirichlet surface thermal condition constrained by 20 m borehole temperatures and annual surface air temperatures. Like many other alpine glaciers, strain heating is an important parameter controlling the englacial thermal structure in LHG12. We suggest that the extent of accumulation basin (the amount of refreezing latent heat from meltwater) of LHG12 may have a considerable impact on the englacial thermal status.

1 Introduction

The storage of water in glaciers is an important component of the hydrological cycle at different time scales (Jansson et al., 2003; Huss et al., 2010), especially in arid and semi-arid regions such as northwestern China, where many glaciers are currently retreating and disappearing (Yao et al., 2012; Neckel et al., 2014; Tian et al., 2014). Located on the northeastern edge of the Tibetan Plateau (36 – 39 °N, 94 – 104 °E), Mt. Qilian Shan (MQS) develops 2051 glaciers covering an area of approximately 1057 km^2 with a total ice volume of approximately 50.5 km^3 (Guo et al., 2014, 2015). Meltwater from MQS glaciers is a very important water resource for the agricultural irrigation and socio-economic development of the oasis cities in northwestern China. Thus, the changes in the MQS glaciers that occur as the climate becomes warmer in the near future are of concern.

Due to logistic difficulties, few MQS glaciers have been investigated in previous decades. However, Laohugou Glacier No.12 (hereafter referred to as LHG12), the largest valley glacier of MQS, has been investigated. Comprised of two branches (east and west), LHG12 is located on the north slope of western MQS (39°27' N, 96°32' E; Fig. 1), with a length of approximately 9.8 km, an area of approximately 20.4 km^2, and an elevation range of 4260 – 5481 m a.s.l. (Liu et al., 2011). LHG12 was first studied by a Chinese expedition from 1958 – 1962 and was considered again in short-term field campaigns in the 1970s and 1980s that were aimed at monitoring glacier changes (Du et al., 2008). Since 2008, the Chinese Academy of Sciences has operated a field station for obtaining meteorological and glaciological measurements of LHG12.

The temperature distribution of a glacier primarily controls the ice rheology, englacial hydrology, and basal sliding conditions (Blatter and Hutter, 1991; Irvine-Fynn et al., 2011; Schäfer et al., 2014). A good understanding of the glacier thermal conditions is important for predicting glacier response to climate change (Wilson et al., 2013; Gilbert et al., 2015), improving glacier hazard analysis (Gilbert et al., 2014a), and reconstructing past climate histories (Vincent et al., 2007; Gilbert et al., 2010). The thermal regime of a glacier is mainly controlled by the surface thermal boundary conditions (e.g., Gilbert et al., 2014b; Meierbachtol et al., 2015). For example, near-surface warming from refreezing meltwater and cooling from the cold air of crevasses influence the thermal regimes of glaciers (Wilson and Flowers, 2013; Wilson et al., 2013; Gilbert et al., 2014a). Using both *in situ* measurements and numerical models, Meierbachtol et al. (2015) argued that shallow borehole ice temperatures served as better boundary constraints than surface air temperatures in Greenland. However, for the east Rongbuk glacier on Mt. Everest, which is considered polythermal, Zhang et al. (2013) found that the modeled ice temperatures agreed well with the *in situ* shallow borehole observations when using surface air temperatures as the surface thermal boundary condition. Therefore, careful investigation of the upper thermal boundary condition is highly necessary for glaciers in different regions under different climate conditions.

LHG12 is widely considered as an extremely continental type (cold) glacier and is characterized by low temperatures and precipitation (Huang, 1990; Shi and Liu, 2000). However, in recent years, we have observed extensive and widespread meltwater on the ice surface and at the glacier terminus. In addition, percolation of snow meltwater consistently occurs in the accumulation basin during the summer. Therefore, we address the following two pressing questions in this study: (i) What is the present thermal status of LHG12? and (ii) How do different surface thermal boundary conditions impact the modeled ice temperature and flow fields? Because temperate ice can assist basal slip and accelerate glacier retreat, understanding the current thermal status of LHG12 is very important for predicting its future dynamic behaviour.

To answer these questions, we conduct diagnostic and transient simulations for LHG12 by using a thermo-mechanically coupled first-order flowband ice flow model. This paper is organized as follows: First, we provide a detailed description of the glaciological datasets of LHG12. Then, we briefly review the numerical ice flow model and the surface mass balance model used in this study. Next, we perform both diagnostic and transient simulations. In the diagnostic simulations, we first investigate the sensitivities of ice flow model parameters, and we then compare the diagnostic results with measured ice surface velocities and ice temperature profile obtained from a deep borehole, and we also explore the impacts of different surface thermal boundary conditions and assess the contributions of heat advection, strain heating, and basal sliding to the temperature field of LHG12. Transient simulations are performed during the period 1961–2013. The evolution of the temperature profile in the deep borehole is then investigated. Finally, we discuss the limitations of our model and present the important conclusions that resulted from this study.

2 Data

Most *in situ* observations, e.g., borehole ice temperatures, surface air temperatures and ice surface velocities, have been made on the east branch (mainstream) of LHG12 (Fig. 1). Measurements on the west branch are sparse and temporally discontinuous. Thus, we only consider the *in situ* data from the east tributary when building our numerical ice flow model.

2.1 Glacier geometry

In July – August 2009 and 2014, two ground-penetrating radar (GPR) surveys were conducted on LHG12 using a pulseEKKO PRO system with center frequencies of 100 MHz (2009) and 50 MHz (2014) (Fig. 1b). Wang et al. (2016) have presented details regarding the GPR data collection and post-processing.

As shown in Fig. 2, the east branch of LHG12 has a mean ice thickness of approximately 190 m. We observed the thickest ice layer (approximately 261 m) at 4864 m a.s.l. Generally, the ice surface of LHG12 is gently undulating, with a mean slope of 0.08°, and the bed of LHG12 shows significant overdeepening in the middle of the center flowline (CL) (Fig. 2). To account for the lateral effects exerted by glacier valley walls in our 2D ice flow model, we parameterize the lateral drag using the glacier half widths. Based on the GPR measurements on LHG12, we parameterize the glacier cross-sections by a power law function $z = aW(z)^b$, where z and $W(z)$ are the vertical and horizontal distances from the lowest point of the profile, and a and b are constants representing the flatness and steepness of the glacier valley, respectively (Svensson, 1959). The b values for LHG12 range from 0.8 to 1.6, indicating that the valley is approximately "V"-shaped (Wang et al., 2016). As an input for the flowband ice flow model, the glacier width, W, was also calculated by ignoring all tributaries (including the west branch) (Fig. 1b and 2).

2.2 Ice surface velocities

The surface velocities of the ice in LHG12 were determined from repeated surveys of stakes drilled into the ice surface. All stakes were located in the distance between km 0.6 – 7.9 along the CL (Fig. 3), spanning an elevation range of 4355 – 4990 m.a.s.l. (Fig. 1b). We measured the stake positions using a real-time kinematic (RTK) fixed solution by a South Lingrui S82 GPS system (Liu et al., 2011). The accuracy of the GPS positioning is an order of a few centimeters and the uncertainty of the calculated ice surface velocties is estimated to be less than 1 m a^{-1}. Because it is difficult to conduct fieldwork on LHG12 (due to, e.g., crevasses and supra-glacial streams), it was nearly impossible to measure all stakes each observational year. Thus, the current dataset includes annual ice surface velocities from 2008 – 2009 and 2009 – 2010, summer measurements from June 17 – August 30, 2008, and winter measurements from February 1 – May 28, 2010.

The *in situ* ice surface velocities shown in Fig. 3 are all from stakes near the CL (Fig. 1b). Small ice surface velocities ($<$ 17 m a^{-1}) are clearly visible in the upper accumulation (km 0 – 1.2) and lower ablation areas (km 6.5 – 9.0) (Fig. 3). Fast ice flow ($>$ 30 m a^{-1}) can be observed between elevations of 4700 – 4775 m a.s.l. (km 4.0 – 5.0), where the ice surface velocities during the summer are approximately 6 m a^{-1} greater than the annual mean velocity ($<$ 40 m a^{-1}). Measurements of winter ice surface velocities ($<$ 10 m a^{-1}) are only available near the glacier terminus showing a clear inter-annual variation of the ice flow speeds.

2.3 Borehole ice temperature

In August 2009 and 2010, we drilled three 25 m deep shallow boreholes on LHG12 (Fig. 1b). One borehole was drilled in the upper ablation area (site 2, approximately 4900 m a.s.l.) and two boreholes were drilled at the AWS locations (sites 1 and 3). The snow/ice temperatures were measured in the boreholes during the period of October 1, 2010 – September 30, 2011. The seasonal variations of the snow/ice temperatures in the shallow boreholes are presented in Figs. 4a, b and c. Our measurements show very little fluctuation ($\pm$0.4 K) in the ice temperatures over the depth range of 20 – 25 m. Below the 3 m depth, the annual mean temperature profiles for sites 1 and 2 show a linearly increase in temperature with depth, while the annual mean temperature profile for site 3 is convex upward. The mean annual 20 m ice temperatures (T_{20m}) at sites 1, 2, and 3 are 5.5 K, 3.0 K, and 9.5 K higher than the mean annual air temperatures (T_{air}), respectively. Despite its higher elevation, the near-surface snow/ice temperatures below a depth of 5 m at site 3 are greater than the near-surface snow/ice temperatures in the ablation area (sites 1 and 2), largely due to the latent heat released as the meltwater entrapped in the surface snow layers refreezes.

To determine the englacial thermal conditions of LHG12, we drilled a deep ice core (167 m) in the upper ablation area of LHG12 (approximately 4971 m a.s.l., Fig. 1b). In October 2011, the ice temperature were measured to a depth of approximately 110 m using a thermistor string after 20 days of the drilling, as shown in Fig. 4d. The string consists of 50 temperature sensors with a vertical spacing of 0.5 m and 10 m at the ice depths of 0 – 20 m and 20 – 110 m, respectively. The accuracy of the temperature sensor is around $\pm$0.05 K (Liu et al., 2009). From Fig. 4d we can see that the temperature profile is close to linear with a temperature gradient of around 0.1 K m^{-1} at the depths of 9 – 30 m. Below the depth of 30 m, the ice temperature demonstrates a linear relationship with depth as well but with a smaller temperature gradient of around 0.034 K m^{-1}.

2.4 Meteorological data

Two automatic weather stations (AWS) were deployed on LHG12, one in the ablation area at 4550 m a.s.l. (site 1, Fig. 1b), and the other in the accumulation area at 5040 m a.s.l. (site 3). During the period of 2010 – 2013, the mean annual air temperatures (2 m above the ice surface) at sites 1 and 3 were $-9.2\,^{\circ}$C and $-12.2\,^{\circ}$C, respectively, indicating a lapse rate of -0.0061 K m^{-1}.

The historical knowledge of the surface air temperature and the ELA of LHG12 is a necessity for running the transient model. We reconstruct the past air temperature on LHG12 based on the observations of the Tuole meteorological station (3367 m a.s.l.), which is approximately 175 km southeast to LHG12. We get the precipitation on LHG12 by downscaling the CAPD (China Alpine Region Month Precipitation Dataset) in Qilian Shan. CAPD provides the monthly sum of precipitation during the period of 1960 – 2013 with a grid spacing of 1 km. We calculate the precipitation on LHG12 from its surrounding 91 grids in CAPD based on the relationship between precipitation and geometric parameters. More details about the reconstruction of both air temperature and precipitation for LHG12 can be found in the Supplement.

3 Thermomechanical ice flow model

In this study, we used the same two-dimensional (2D), thermo-mechanically coupled, first-order, flowband ice flow model as in Zhang et al. (2013). Therefore, we only address a very brief review of the model here.

3.1 Ice flow model

We define x, y, and z as the horizontal along-flow, horizontal across-flow and vertical coordinates, respectively. By assuming the vertical normal stress as hydrostatic and neglecting the bridging effects (Pattyn, 2002), the equation for momentum balance is given as

$$\frac{\partial}{\partial x}(2\sigma'_{xx} + \sigma'_{yy}) + \frac{\partial \sigma'_{xy}}{\partial y} + \frac{\partial \sigma'_{xz}}{\partial z} = \rho g \frac{\partial s}{\partial x}, \tag{1}$$

where σ'_{ij} is the deviatoric stress tensor, ρ is the ice density, g is the gravitational acceleration, and s is the ice surface elevation. The parameters used in this study are given in Table 1.

The constitutive relationship of ice dynamics is described by the Glen's flow law (Cuffey and Paterson, 2010)

$$\sigma'_{ij} = 2\eta\dot{\epsilon}_{ij}, \quad \eta = \frac{1}{2}A^{-1/n}(\dot{\epsilon_e} + \dot{\epsilon}_0)^{(1-n)/n}, \tag{2}$$

where η is the ice viscosity, $\dot{\epsilon}_{ij}$ is the strain rate, n is the flow law exponent, A is the flow rate factor, $\dot{\epsilon_e}$ is the effective strain rate, and $\dot{\epsilon}_0$ is a small number used to avoid singularity. The flow rate factor is parameterized using the Arrhenius relationship as

$$A(T) = A_0 \exp(-\frac{Q}{RT}), \tag{3}$$

where A_0 is the pre-exponential constant, Q is the activation energy for creep, R is the universal gas constant, and T is the ice temperature. The effective strain rate $\dot{\epsilon_e}$ is related to the velocity gradient by

$$\dot{\epsilon}_e^2 \simeq \left(\frac{\partial u}{\partial x}\right)^2 + \left(\frac{\partial v}{\partial y}\right)^2 + \frac{\partial u}{\partial x}\frac{\partial v}{\partial y} + \frac{1}{4}\left(\frac{\partial u}{\partial y}\right)^2 + \frac{1}{4}\left(\frac{\partial u}{\partial z}\right)^2, \tag{4}$$

where u and v are the velocity components along the x and y direction, respectively. By assuming $\partial v/\partial y = (u/W)(\partial W/\partial x)$, we parameterize the lateral drag, σ'_{xy}, as a function of the flowband half width, W, following Flowers et al. (2011)

$$\sigma'_{xy} = -\frac{\eta u}{W}. \tag{5}$$

For an easy numerical implementation, we reformulate the momentum balance equation (1) as

$$\frac{u}{W}\left\{2\frac{\partial\eta}{\partial x}\frac{\partial W}{\partial x}+2\eta\left[\frac{\partial^2 W}{\partial x^2}-\frac{1}{W}\left(\frac{\partial W}{\partial x}\right)^2\right]-\frac{\eta}{W}\right\}$$
$$+\frac{\partial u}{\partial x}\left(4\frac{\partial\eta}{\partial x}+\frac{2\eta}{W}\frac{\partial W}{\partial x}\right)+\frac{\partial u}{\partial z}\frac{\partial\eta}{\partial z}+4\eta\frac{\partial^2 u}{\partial x^2}+\eta\frac{\partial^2 u}{\partial z^2}=\rho g\frac{\partial s}{\partial x}, \tag{6}$$

where the ice viscosity is defined as

$$\eta=\frac{1}{2}A^{-1/n}\left[\left(\frac{\partial u}{\partial x}\right)^2+\left(\frac{u}{W}\frac{\partial W}{\partial x}\right)^2+\frac{u}{W}\frac{\partial u}{\partial x}\frac{\partial W}{\partial x}+\frac{1}{4}\left(\frac{\partial u}{\partial z}\right)^2+\frac{1}{4}\left(\frac{u}{W}\right)^2+\dot{\epsilon}_0^2\right]^{(1-n)/2n}. \tag{7}$$

3.2 Ice temperature model

The ice temperature field can be calculated using a 2D heat transfer equation (Pattyn, 2002),

$$\frac{\partial T}{\partial t}=\frac{k}{\rho c_p}\left(\frac{\partial^2 T}{\partial x^2}+\frac{\partial^2 T}{\partial z^2}\right)-\left(u\frac{\partial T}{\partial x}+w\frac{\partial T}{\partial z}\right)+\frac{4\eta\dot{\epsilon}_e{}^2}{\rho c_p}, \tag{8}$$

where w is the vertical ice velocity, k and c_p are the thermal conductivity and heat capacity of the ice, respectively.

The pressure melting point of the ice, T_{pmp}, is described by the Clausius-Clapeyron relationship

$$T_{\text{pmp}}=T_0-\beta(s-z), \tag{9}$$

where T_0 is the triple-point temperature of water and β is the Clausius-Clapeyron constant. Following Zhang et al. (2013), we determined the position of the cold-temperate ice transition surface (CTS) by considering the following two cases: (i) melting condition, i.e., cold ice flows downward into the temperate ice zone, and (ii) freezing condition, i.e., temperate ice flows upward into the cold ice zone (Blatter and Hutter, 1991; Blatter and Greve, 2015). For the melting case, the ice temperature profile at the CTS simply follows a Clausius-Clapeyron gradient (β). However, for the freezing case, the latent heat, Q_r, that is released when the water contained in the temperate refreezes is determined as (Funk et al., 1994)

$$Q_r=\mu w\rho_w L, \tag{10}$$

where μ is the fractional water content of the temperate ice, ρ_w is the water density and L is the latent heat of freezing. In this case, following (Funk et al., 1994), the ice temperature gradient at the CTS can be described as

$$\frac{\partial T}{\partial z}=-\frac{Q_r}{k}+\beta. \tag{11}$$

3.3 Free surface

The free surface evolution follows the kinematic boundary equation,

$$\frac{\partial s}{\partial t}=b_n+w_s-u_s\frac{\partial s}{\partial x}, \tag{12}$$

where $s(x,t)$ is the free surface elevation, u_s and w_s are the surface velocity components in x and z, and b_n is the surface mass balance.

3.4 Boundary conditions

3.4.1 Boundary conditions for ice flow model

For the ice flow model, we assume a stress-free condition for the glacier surface, and use the Coulomb friction law to describe the ice-bedrock interface where the ice slips (Schoof, 2005),

$$\tau_b = \Gamma\left(\frac{u_b}{u_b + \Gamma^n N^n \Lambda}\right)^{1/n} N, \qquad \Lambda = \frac{\lambda_{\text{max}} A}{m_{\text{max}}}, \tag{13}$$

where τ_b and u_b are the basal drag and velocity, respectively, N is the basal effective pressure, λ_{max} is the dominant wavelength of the bed bumps, m_{max} is the maximum slope of the bed bumps, and Γ and Λ are geometrical parameters (Gagliardini et al., 2007). Here we take $\Gamma = 0.84 m_{\text{max}}$ following Flowers et al. (2011) and Zhang et al. (2013). The basal effective pressure in the friction law, N, is defined as the difference between the ice overburden pressure and the basal water pressure (Gagliardini et al., 2007; Flowers et al., 2011),

$$N = \rho g H - P_w = \phi \rho g H, \tag{14}$$

where H and P_w are the ice thickness and basal water pressure, respectively, and ϕ implies the ratio of basal effective pressure to the ice overburden pressure. The basal drag is defined as the sum of all resistive forces (Van der Veen, 1989; Pattyn, 2002). It should be noted that the basal sliding is only permitted when basal ice temperature reaches the local pressure-melting point.

3.4.2 Boundary conditions for ice temperature model

We apply a Dirichlet temperature constraint (T_{sbc}) on the ice surface in the temperature model. In some studies, $T_{\text{sbc}} = T_{\text{air}}$ is used (e.g. Zhang et al., 2013), which, as suggested by recent studies, could result in lower velocity values (Sugiyama et al., 2014) and cold bias in ice temperature simulations (Meierbachtol et al., 2015). By contrast, Meierbachtol et al. (2015) recommended using the near-surface temperature T_{dep} at depth where inter-annual variations of air temperatures are damped (15 – 20 m deep) (a proxy for the annual mean ice surface temperature). One advantage of using T_{dep} is that the effects of refreezing meltwater and the thermal insulation of winter snow can be included in the model (Huang et al., 1982; Cuffey and Paterson, 2010). In fact, the condition $T_{\text{dep}} = T_{\text{air}}$ is acceptable only in dry and cold snow zones (Cuffey and Paterson, 2010); however, $T_{\text{dep}} > T_{\text{air}}$ is often observed in zones where meltwater is refreezing in glaciers, such as the LHG12 (Fig. 4). In this study, we set T_{sbc} in the accumulation zone to the glacier near-surface temperature T_{dep}, while T_{sbc} in the ablation area is prescribed by a simple parameterization (Lüthi and Funk, 2001; Gilbert et al., 2010) as

$$T_{\text{sbc}} = \begin{cases} T_{\text{dep}}, & s > ELA, \\ T_{\text{air}} + c, & s \leq ELA, \end{cases} \tag{15}$$

where ELA is the equilibrium-line altitude, and c is a tuning parameter implicitly accounting for effects of the surface energy budget and the lapse rate of air temperature (Gilbert et al., 2010). We denote Eq. (15) as the surface thermal boundary condition of the reference experiment (E-ref) after comparing another numerical experiment by setting $T_{\text{sbc}} = T_{\text{air}}$ (E-air) (see Sect. 6.1.3 for details).

At the ice-bedrock interface, we apply the following Neumann-type boundary condition in the temperature model,

$$\frac{\partial T}{\partial z} = -\frac{G}{k}, \tag{16}$$

where G is the geothermal heat flux. We here use a constant geothermal heat flux, 40 mW m^{-2}, an *in situ* measurement from the Dunde ice cap in the western MQS (Huang, 1999), over the entire model domain.

3.5 Numerical solution

In our model we use a finite difference discretization method and a terrain-following coordinate transformation. The numerical mesh we use contains 61 grid points in x and 41 layers in z. The ice flow model (Eq. (6)) is discretized with a second-order centered difference scheme while the ice temperature model (Eq. (8)) employs a first-order upstream difference scheme for the horizontal heat advection term and a node-centered difference scheme for the vertical heat advection term and the heat diffusion terms. The velocity and temperature fields are iteratively solved by a relaxed Picard subspace iteration scheme (De Smedt et al., 2010) in Matlab. The free surface evolution (Eq. (12)) is solved using a Crank-Nicolson scheme. More details are given in Zhang et al. (2013).

4 Surface mass balance model

In our parameterization of the surface thermal boundary condition, a transient ELA is important in controlling the extent of accumulation zone which can be largely warmed by the refreezing of meltwater. We estimate the annual surface mass balance b_n of LHG12 between 1960 and 2013, and find the location of ELA by $b_n = 0$.

The daily ablation at elevation z, $a(z)$, is calculated based on a degree-day method (Braithwaite and Zhang, 2000):

$$a(z) = f_m \mathrm{PDD}(z), \tag{17}$$

where f_m is the degree-day factor, and PDD is the daily positive degree-day sum for glacier surface melt,

$$\mathrm{PDD} = T_{\text{mean}} - T_m, \tag{18}$$

where T_{mean} is the daily mean air temperature, and T_m is the threshold temperature when melt occurs. Note that surface melt may happen even if $T_{\text{mean}} < 0\,^{\circ}\mathrm{C}$, due to the positive air temperature during the day, indicating a negative T_m in such cases.

As the CAPD dataset only provides monthly precipitation sums, we estimate the daily precipitation on LHG12 by assuming a uniformly distributed precipitation over a month. The daily accumulation at elevation z, $c(z)$ is calculated as follows,

$$c(z) = \begin{cases} f_P \cdot P_{\text{total}}, & T_{\text{mean}} < T_{\text{crit1}}, \\ f_P \cdot \frac{T_{\text{crit2}} - T_{\text{mean}}}{T_{\text{crit2}} - T_{\text{crit1}}} \cdot P_{\text{total}}, & T_{\text{crit1}} \leq T_{\text{mean}} \leq T_{\text{crit2}}, \\ 0, & T_{\text{mean}} > T_{\text{crit2}}, \end{cases} \tag{19}$$

where P_{total} is the daily precipitation, T_{crit1} and T_{crit2} are the threshold temperatures for the snow and rain transition, and f_P is a tuning parameter for the precipitation to account for the uncertainties of the gridded CAPD data and the downscaling method. The model is well calibrated by investigating the sensitivities of model parameters and by comparing the simulated results with the observed mass balance in 2010–12 (See details in the Figs. S5–8 in the Supplement).

5 Simulation strategies

5.1 Surface relaxation

In order to remove the uncertainties remained in the model initial conditions (including initial topography and model parameters) (Zwinger and Moore, 2009; Seroussi et al., 2013), we allow the free surface to relax for a period of 3 years assuming zero surface mass balance and basal sliding (See details in the Supplement). The time step for the relaxation experiment is set to 0.1 year. We apply surface relaxation before running all of the diagnostic and transient simulations in this paper.

5.2 Diagnostic simulations

In our diagnostic simulations, we assume a thermal steady-state condition and use the relaxed present-day geometry of LHG12. First, we explore the model sensitivities to geometrical bed parameters (λ_{max} and m_{max}), ratio of basal effective pressure (ϕ), water content (μ), geothermal heat flux (G), and the valley shape index (b). Next, we tune the surface thermal boundary condition parameters, i.e., ELA, T_{dep} and c to fit the modeled steady-state temperature profile to observations in the deep borehole (Fig. 1). We then investigate the modeled horizontal velocity field and thermal structure of LHG12, and compare the diagnostic simulation results with observations. We also perform experiments to investigate sensitivity of the thermomechanical model to different surface thermal boundary conditions (E-ref and E-air). Finally, we perform four experiments (E-advZ, E-advX, E-strain, and E-slip) to explore the effects of heat advection, strain heating, and basal sliding on the thermal distribution and flow dynamic behaviours of LHG12.

5.3 Transient simulations

To investigate the impacts of historical climate conditions on the thermal regime of LHG12, time-dependent simulations are performed from 1961 to 2011. In our simulations, we assume that the surface temperature (T_{dep}) in the accumulation zone is constant in time and space. Due to a lack of in-situ observations (e.g. firn thickness, firn densities) and coupled heat-water transfer model (e.g. Gilbert, 2012; Wilson, 2013), we do not simulate the complex processes of heat exchange in the accumulation zone. To understand how the thermal status varies over time in the deep borehole, we design three (cold, warm and reference) transient simulations by setting T_{dep} to $-5\,^{\circ}\text{C}$, $-1\,^{\circ}\text{C}$ and $-2.1\,^{\circ}\text{C}$ (as calibrated in our steady state simulations; see Sect. 6.1.1), respectively.

In the transient model, the ice surface temperature (T_{sbc}) and ELA are allowed to vary in time. However, we keep the glacier geometry fixed in the transient simulations for the following two reasons: 1) The tributaries of LHG12, which our flowband model neglects, may have non-negligible inflow ice fluxes that impact the mass continuity equation; 2) The mean surface elevation change above 4600 m a.s.l. (the confluence area) over 1957–2014 is close to negligible (approximately -10.4 m, around 4.4% of the ice thickness) (See Fig. S10 in the Supplement). Before we run the transient experiments, we perform a 10-year spin-up using the mean values of surface air temperatures and ELAs during 1961–1970.

6 Simulation results and discussions

6.1 Diagnostic simulations

6.1.1 Parameter sensitivity

As shown in Figs. 5 and 6, we conduct a series of sensitivity experiments to investigate the relative importance of different model parameters ($\lambda_{\max}$, $m_{\max}$, ϕ, μ, G, b) on ice flow speeds and temperate ice zone (TIZ) sizes by varying the value of one parameter while holding the others fixed. We set ELA to 4980 m a.s.l., as observed in the 2011 remote sensing image of LHG12. T_{dep} and c are set to -2.7 °C and -4.3 °C, which are calculated from the 20 m deep ice temperatures and mean annual air temperatures for the two shallow boreholes in the accumulaiton basin, respectively.

The friction law parameters, $\lambda_{\max}$ and $m_{\max}$, which describe the geometries of bedrock obstacles (Gagliardini et al., 2007; Flowers et al., 2011), have non-negligible impacts on the model results. As shown in Figs. 5a and b, the modeled velocities and TIZ sizes increase as $\lambda_{\max}$ increases and $m_{\max}$ decreases, similar to the results observed by Flowers et al. (2011) and Zhang et al. (2013). A large increase in the modeled basal sliding velocity occurs when $m_{\max}$ is lower than 0.2. The ratio, ϕ, is an insensitive parameter in our model when it is larger than 0.3 (Fig. 5c). Although the water content, μ, in the ice does not directly impact the ice velocity simulations (the flow rate factor A is assumed independent of the water content in ice), the water content can affect the temperature field and, consequently, influence A and the ice velocities (Fig. 5d). Fig. 6d shows that increasing the water content may result in larger TIZ sizes. In addition, we test the sensitivity of the model to different geothermal heat flux values. A larger geothermal heat flux can result in larger TIZs but has a limited impact on modeling ice velocity (Figs. 5e and 6e). As shown by Zhang et al. (2013), our model results are mainly controlled by the shape of the glacial valley, specifically the b index (Sect. 2.1). A large value of b indicates a flat glacial valley and suggests that a small lateral drag was exerted on the ice flow (Figs. 5f and 6f).

Based on the sensitivity experiments described above, we adopt a parameter set of $\lambda_{\max} = 4$ m, $m_{\max} = 0.3$, $\phi = 1$ (no basal water pressure), $\mu = 3\%$, $G = 40$ mW m^{-2}, and $b = 1.2$ as a diagnostic reference in our modeling experiment (E-ref). For a better fitting to the observed ice temperature in the deep borehole, we further tune the parameters ELA, T_{dep} and c by a series of model runs using the above parameter set. The performance of different parameter combinations is evaluated by comparing the root-mean-squres (RMS) of the differences between the measured and modeled temperature profiles for the deep borehole (Fig. 7). We find the RMS sufficiently small when ELA = 4990 m a.s.l., $T_{\text{dep}} = -2.1\,°\text{C}$, and $c = 4\,°\text{C}$, close to observations. By doing this we argue that the transient climate information of the past is partly included in the tuned parameters in our diagnostic simulations.

6.1.2 Comparison with *in situ* observations

In the reference experiment (E-ref), we diagnostically simulate the distributions of horizontal ice velocities and temperatures (Figs. 8a and c). Next, the model results are compared to the measured ice surface velocities and the ice temperature profile in the deep borehole (Figs. 8b and d). Generally, the modeled ice surface velocities are in good agreement with *in situ* observations from the glacier head to km 4.8 along the CL (Fig. 8b). However, from km 4.8 to the glacier terminus, our model generally underestimates the ice surface velocities as shown in all simulations in Fig. 5. There are three possilbe reasons for this underestimation. First, the model neglects the convergent ice fluxes from the west branch. Second, an enhanced basal sliding zone may exist at the confluence area, which is not captured by the model. In addition, the diagnostic model using fixed topography cannot capture the time-dependent glacier changes which can largely influence the ice flow dynamics. Here we verify the first two hypotheses by conducting two other experiments, E-W and E-WS. In E-W the glacier widths are increased by 450 m at km 5.8 – 7.3 as a proxy of including the impact of the convergent flow from the west branch (Fig. 9). In E-WS, except for the same glacier width increasing as in E-W, we also increase λ_{max} by 100% and decrease m_{max} by 33% for accelerating the basal sliding at km 5.8 – 7.3 (Fig. 9). We can clearly find that while both factors have a non-negligible contribution to the model results, the basal sliding may play a bit more important role in the confluence area. This indicates a need of considering glacier flow branches and spatially variable sliding law parameters in real glacier modeling studies.

The model predicts a TIZ overlain by cold ice over a horizontal distance of km 0.6 – 7.4 (Fig. 8c). In addition, we further compare our model results with the *in situ* 110 m deep ice temperature measurements (Fig. 8d). Modeled and measured borehole temperature profiles show a close match within a root-mean-square difference of 0.3 K below the 10 m depth. Because *in situ* ice temperature data from below 110 m have not been obtained, we were unable to compare the modeled and measured ice temperatures at the ice-bedrock interface. Glacier thermal regime is largely influenced by the climate history and firn thickness (Gilbert et al., 2012, 2014a). However, our diagnostic simulation assumes a thermal steady-state and applies a simple thermal boundary condition. The good agreement between modeled and measured temperature profiles is likely due that we selecte a snow line altitude representing a steady state for the glacier mass balance, and the surface thermal boundary condition includes the effect of refreezing meltwater in the accumulation zone.

6.1.3 Choice of surface thermal boundary condition

To investigate the impacts of different surface thermal boundary conditions on the thermo-mechanical fields of LHG12, we perform an experiment (E-air) in which we set $T_{\text{sbc}} = T_{\text{air}}$, and compare its results with those of E-ref.

Fig. 10 shows that the ice temperatures along the CL are highly sensitive to T_{sbc}. From E-air, it is observed that LHG12 becomes fully cold, with an average field temperature 6.5 K colder than that of E-ref (Fig. 10a), which decreases the ice surface velocity by approximately 10.0 m a^{-1} (Fig. 10b). In contrast to the measured deep borehole temperature profile at site 3, E-air results in an unreliable temperature profile that is much colder than the actual temperatures at all depths.

As noted above, the dynamics of LHG12 can be strongly influenced by the choices of different surface thermal boundary conditions. For LHG12, most accumulation and ablation events overlap during the summer season (Sun et al., 2012). The meltwater entrapped in snow and moulins during the summer season can release large amounts of heat due to refreezing when the temperature decreases, which may significantly increase the ice temperatures in the near-surface snow/ice layers (Fig. 4) and result in the warm bias of T_{20m} (compared with the mean annual surface air temperature). Therefore, compared with E-air, the experiment E-ref better incorporate the effects of meltwater refreezing in the accumulation basin into the prescribed surface thermal boundary constraints resulting in more accurate simulations of ice temperature and flow fields.

6.1.4 Roles of heat advection, strain heating and basal sliding

To assess the relative contributions of heat advection and strain heating to the thermo-mechanical field of LHG12, we conducted three experiments (E-advZ, E-advX, and E-strain), in which the vertical advection, horizontal along-flow advection and strain heating were neglected, respectively. In addition, to investigate the effects of basal sliding predicted by the Coulomb friction law on the thermal state and flow dynamics of LHG12, we performed an experiment (E-slip) with $u_b = 0$.

Figs. 10 and 11 compare the ice velocity and temperature results of E-advZ, E-advX, E-strain and E-slip with those of E-ref. If the vertical advection is neglected (E-advZ; cold ice at the glacier surface cannot be transported downwards into the interior of LHG12), LHG12 becomes warmer (Figs. 10a and c) and flows faster relative to other experiments (Fig. 10b). As described for the discontinuous surface thermal boundary conditions across the ELA (a straightforward result from the refreezing meltwater in the accumulation basin), a discontinuous transition of the mean column ice temperature is observed along the CL at km 1.3 (the horizontal position of ELA) in E-advX (Fig. 10a). Compared with E-ref, the E-advX experiment predicts colder field temperatures (by approximately 2.0 K) and much smaller surface ice velocities. Because the accumulation basin of LHG12 is relatively warm, E-advX, which neglects the horizontal transport of ice from upstream and downstream, predicts much colder conditions for LHG12, i.e., the modeled temperate ice only appears at two discontinuous grid points (Fig. 10c). As described by Zhang et al. (2015), we observed that strain heating contributes greatly to the thermal configuration of LHG12. If we leave away the strain heating (E-strain), LHG12 becomes fully cold, with a mean ice temperature field lower than that of E-ref by approximately 0.5 K. Previous studies have suggested that basal sliding can significantly influence the thermal structures and velocity fields of glaciers (Wilson et al., 2013; Zhang et al., 2015, e.g.). However, in this study the neglect of basal sliding (E-slip) results in a temperature field very similar to that of E-ref. We attribute this difference to the relatively small modeled basal sliding values for LHG12. The observed and modeled ice temperature profiles of E-advZ, E-advX, E-strain, E-slip, and E-ref are also compared for the deep ice borehole in Figs. 10d and 11d. The differences of the profiles can also be explained by our above explanations.

6.2 Transient simulations

As can be clearly seen from Figure 12a, the temperature profile in the deep borehole can be remarkably determined by two factors, the thermal condition (T_{dep}) and the extent (ELA) of the accumulation basin. T_{dep} directly impacts the upstream surface thermal boundary condition of LHG12, while ELA controls the heat conduction near the deep borehole by varing the extent of accumulation basin and thus the amount of refreezing heat of melt water. In Figure 12a, the cold (warm) case underestimates (overestimates) the ice temperature in the deep borehole, compared with the observation. The reference case, which adopts the tuned vaule of T_{dep} ($-2.1\,^{\circ}$C) for the diagnostic experiment, shows a good agreement between the modeled and observed temperature profile, suggesting a possibly supportive evidence that the calibrated T_{dep} for the diagnostic simulation might indeed contain part of the historical climate information of LHG12. In Figure 12b, we can see that both the summer (June, July and August) air temperature and ELA appear a slight (large) increase during 1971–1991 (1991–2011), which can explain the small (large) decrease of ice temperatures for all model cases over the same time period, indicating that LHG12 (or similar type glaciers) may not accordingly become cold under a cold climate scenario, when a relatively large accumulaiton basin grows and more refreezing latent heat from meltwater is released. In addition, a comparison of vertically averaged ice velocity and temperature field between the diagnostic and transient (reference case) simulations is presented in Figure 12c and d. In general, the pattern of the velocity profiles shows the opposite to that of the temperature profiles. For example, the diagnostic velocity (temperature) are larger (smaller) than the transient result over the horizontal distances of km 0–1.8 and km 8–9.8. The transient model appears to bring more heat from the accumulation basin to downtream over the past decades.

6.3 Model limitations

Although our 2D, first-order, flowband model can account for part of the three-dimensional nature of LHG12 by parameterizing the lateral drag with glacier width variations, it cannot fully describe the ice flow along the y direction, and are not able to account for the confluence of glacier tributaries. The shape of the LHG12 glacier valley is described using a constant value for index b (1.2; approximately "V" type cross-sections), which was determined from several traverse GPR profiles (Fig. 1). However, for real glaciers, the cross-sectional geometry profiles are generally complex, resulting in an inevitable bias when we idealize the glacier cross-sectional profiles by using power law functions across the entire LHG12. Although the regularized Coulomb friction law provides a physical relationship between the basal drag and sliding velocities, several parameters (e.g., λ_{max}, m_{max}) still must be prescribed based on surface velocity observations. Another uncertainty could be from the spatially uniform geothermal heat flux that we assume in the model, as it may have a great spatial variation due to mountain topography (Lüthi and Funk, 2001). In addition, we can also improve our model ability by linking the water content in the temperate ice layer to a physical thermo-hydrological process in the future.

Due to the limitations of *in situ* shallow borehole ice temperature measurements, the surface thermal boundary condition in our temperature model is determined using a simple parameterization based on observations at three elevations (Fig. 1b). In addition, the parameterized surface thermal boundary condition only provides a rough estimate of the overall contributions of the heat from refreezing meltwater and ice flow advection. At this stage, we cannot simulate the actual physical process involved in the transport of near-surface heat from refreezing, which has been suggested by Gilbert et al. (2012); Wilson and Flowers (2013). Because of the uncertainties of the knowledge of past climate and glacier geometry, we here do not include the complete transient simulations of LHG12, but instead we carefully calibrate our diagnostic model parameters as a proxy of implicitly representing the impacts of past climate, which may also lead to some unphysical model outputs. Because of the uncertainties of historical climate and geometry inputs, the transient simulations in this paper are mainly for seeking some possible reasons for the formation of the current temperature profile of the deep borehole. We do not expect accurate model results from the transient experiments.

7 Conclusions

For the first time, we investigate the thermo-mechanical features of a typical valley glacier, Laohugou Glacier No.12 (LHG12), in Mt. Qilian Shan, which is an important fresh water source for the arid regions in western China. We assess the thermo-mechanical features of LHG12 using a two-dimensional thermo-mechanically coupled first-order flowband model based on available *in situ* measurements of glacier geometries, borehole ice temperatures, and surface meteorological and velocity observations.

Similar to other alpine land-terminating glaciers, the mean annual horizontal ice flow speeds of LHG12 are relatively low (less than 40 m a^{-1}). However, we observed large inter-annual variations in the ice surface velocity during the summer and winter seasons. Due to the release of heat from refreezing meltwater, the observed ice temperatures for the shallow ice borehole in the accumulation basin (site 3; Fig. 1) are higher than for the temperatures at sites 1 and 2 at lower elevations, indicating the existence of meltwater refreezing, as observed in our field expeditions. Thus, we parameterize the surface thermal boundary condition by accounting for the 20 m deep temperature instead of only the surface air temperatures. We observed that LHG12 has a polythermal structure with a temperate ice zone that is overlain by cold ice near the glacier base throughout a large region of the ablation area. Time-dependent simulations reveal that the englacial temperature becomes colder in recent two decades as a consequence of the shrink of accumulation area and rising surface air temperature.

Horizontal heat advection is important on LHG12 for bringing the relatively warm ice in the accumulation basin (due to the heat from refreezing meltwater) to the downstream ablation zone. In addition, vertical heat advection is important for transporting the near-surface cold ice downwards into the glacier interior, which “cools down” the ice temperature. Furthermore, we argue that the strain heating of LHG12 also plays an important role in controlling the englacial thermal status, as suggested by Zhang et al. (2015). However, we also observed that simulated basal sliding contributes little to the thermal-mechanical configuration of LHG12 (very small; < 4 m a^{-1}).

The mean annual surface air temperature could serve as a good approximation for the temperatures of shallow ice, where seasonal climate variations are damped at cold and dry locations (Cuffey and Paterson, 2010). However, for LHG12, using the mean annual surface air temperature as the thermal boundary condition at the ice surface would predict an entirely cold glacier with very small ice flow speeds. For LHG12, a decline of ELA under a cold climate may assist an increase of the amount of refreezing latent heat in the accumulation basin, and therefore possibly raise the englacial temperature. Because warming is occurring on alpine glaciers in, for example, Mt. Himalayas and Qilian Shan, further studies of supra-glacial and near-surface heat transport are very important because they will affect the surface thermal conditions and, eventually, the dynamical behaviours of the glacier.

Acknowledgements. This work is supported by the National Basic Research Program (973) of China (2013CBA01801, 2013CBA01804), and the Technology Services Network Program (STS-HHS Program) of Cold and Arid Regions Environmental and Engineering Research Institute, Chinese Academy of Sciences (HHS-TSS-STS-1501). We are grateful to numerous people for their hard fieldwork. We thank the supports from the Qilian Shan Station of Glaciology and Ecologic Environment, Chinese Academy of Sciences (CAS). We thank Dr. Chen

Rensheng and Dr. Liu Junfeng for providing the CAPD precipitation dataset. We thank Martin Lüthi and an anonymous reviewer for their thorough and constructive reviews which significantly improved the manuscript, as well as Oliver Gagliardini for his editorial work.

References

Blatter, H. and Greve, R.: Comparison and verification of enthalpy schemes for polythermal glaciers and ice sheets with a one-dimensional model, Polar Science, 9, 196–207, 2015.

Blatter, H. and Hutter, K.: Polythermal conditions in Arctic glaciers, Journal of Glaciology, 37, 261–269, 1991.

Braithwaite, R. J. and Zhang, Y.: Sensitivity of mass balance of five Swiss glaciers to temperature changes assessed by tuning a degree-day model, Journal of Glaciology, 46, 7–14, doi:doi:10.3189/172756500781833511, 2000.

Cuffey, K. and Paterson, W.: The Physics of Glaciers, Elsevier, Amsterdam, 4^{th} edn., 2010.

De Smedt, B., Pattyn, F., and De Groen, P.: Using the unstable manifold correction in a Picard iteration to solve the velocity field in higher-order ice-flow models, Journal of Glaciology, 56, 257–261, 2010.

Du, W., Qin, X., Liu, Y., and Wang, X.: Variation of the Laohugou Glacier No.12 in the Qilian Mountains. (in Chinese with English summary), Journal of Glaciology and Geocryology, 30, 373–379, 2008.

Flowers, G. E., Roux, N., Pimentel, S., and Schoof, C. G.: Present dynamics and future prognosis of a slowly surging glacier, The Cryosphere, 5, 299–313, 2011.

Funk, M., Echelmeyer, K. A., and Iken, A.: Mechanisms of fast flow in Jakobshavn Isbræ, West Greenland: Part II. Modeling of englacial temperatures, Journal of Glaciology, 40, 569–585, 1994.

Gagliardini, O., Cohen, D., Råback, P., and Zwinger, T.: Finite-element modeling of subglacial cavities and related friction law, Journal of Geophysical Research, 112, F02 027, 2007.

Gilbert, A., Wagnon, P., Vincent, C., Ginot, P., and Funk, M.: Atmospheric warming at a high-elevation tropical site revealed by englacial temperatures at Illimani, Bolivia (6340 m above sea level, 16°S, 67°W), Journal of Geophysical Research, 115, D10 109, 2010.

Gilbert, A., Vincent, C., Wagnon, P., Thibert, E., and Rabatel, A.: The influence of snow cover thickness on the thermal regime of Tête Rousse Glacier (Mont Blanc range, 3200 m a.s.l.): Consequences for outburst flood hazards and glacier response to climate change, Journal of Geophysical Research, 117, 2012.

Gilbert, A., Gagliardini, O., Vincent, C., and Wagnon, P.: A 3-D thermal regime model suitable for cold accumulation zones of polythermal mountain glaciers, Journal of Geophysical Research: Earth Surface, 119, 1876–1893, 2014a.

Gilbert, A., Vincent, C., Six, D., Wagnon, P., Piard, L., and Ginot, P.: Modeling near-surface firn temperature in a cold accumulation zone (Col du Dôme, French Alps): from a physical to a semi-parameterized approach, The Cryosphere, 8, 689–703, 2014b.

Gilbert, A., Vincent, C., Gagliardini, O., Krug, J., and Berthier, E.: Assessment of thermal change in cold avalanching glaciers in relation to climate warming, Geophysical Research Letters, 42, 6382–6390, 2015.

Guo, W., Xu, J., Liu, S., Shangguan, D., Wu, L., Yao, X., Zhao, J., Liu, Q., Jiang, Z., Li, P., Wei, J., Bao, W., Yu, P., Ding, L., Li, G., Ge, C., and Wang, Y.: The second glacier inventory dataset of China (Version 1.0), Cold and Arid Regions Science Data Center at Lanzhou, 2014.

Guo, W., Liu, S., Xu, J., Wu, L., Shangguan, D., Yao, X., Wei, J., Bao, W., Yu, P., Liu, Q., and Jiang, Z.: The second Chinese glacier inventory: data, methods and results, Journal of Glaciology, 61, 357–372, 2015.

Huang, M.: On the temperature distribution of glaciers in China, Journal of Glaciology, 36, 210–216, 1990.

Huang, M.: Forty year's study of glacier temperature in China. (in Chinese with English summary), Journal of Glaciology and Geocryology, 21, 193–199, 1999.

Huang, M., Wang, Z., and Ren, J.: On the temperature regime of continental-type glaciers in China, Journal of Glaciology, 28, 117–128, 1982.

Huss, M., Jouvet, G., Farinotti, D., and Bauder, A.: Future high-mountain hydrology: a new parameterization of glacier retreat, Hydrology and Earth System Sciences, 14, 815–829, 2010.

Irvine-Fynn, T. D. L., Hodson, A. J., Moorman, B. J., Vatne, G., and Hubbard, A. L.: Polythermal glacier hydrology: A review, Reviews of Geophysics, 49, 2011.

Jansson, P., Hock, R., and Schneider, T.: The concept of glacier storage: a review, Journal of Hydrology, 282, 116–129, 2003.

Liu, Y., Hou, S., Wang, Y., and Song, L.: Distribution of borehole temperature at four high-altitude alpine glaciers in Central Asia, Journal of Mountain Science, 6, 221–227, 2009.

Liu, Y., Qin, X., Du, W., Sun, W., and Hou, D.: The movement features analysis of Laohugou Glacier No.12 in Qilian Mountains, Sciences in Cold and Arid Regions, 3, 119–123, 2011.

Lüthi, M. P. and Funk, M.: Modelling heat flow in a cold, high-altitude glacier: interpretation of measurements from Colle Gnifetti, Swiss Alps, Journal of Glaciology, 47, 314–324, 2001.

Meierbachtol, T. W., Harper, J. T., Johnson, J. V., Humphrey, N. F., and Brinkerhoff, D. J.: Thermal boundary conditions on western Greenland: Observational constraints and impacts on the modeled thermomechanical state, Journal of Geophysical Research: Earth Surface, 120, 623–636, 2015.

Neckel, N., Kropáček, J., Bolch, T., and Hochschild, V.: Glacier mass changes on the Tibetan Plateau 2003–2009 derived from ICESat laser altimetry measurements, Environmental research letters, 9, 014 009, 2014.

Pattyn, F.: Transient glacier response with a higher-order numerical ice-flow model, Journal of Glaciology, 48, 467–477, 2002.

Schäfer, M., Gillet-Chaulet, F., Gladstone, R., Pettersson, R., A. Pohjola, V., Strozzi, T., and Zwinger, T.: Assessment of heat sources on the control of fast flow of Vestfonna ice cap, Svalbard, The Cryosphere, 8, 1951–1973, 2014.

Schoof, C.: The effect of cavitation on glacier sliding, Royal Society of London Proceedings Series A, 461, 609–627, 2005.

Seroussi, H., Morlighem, M., Rignot, E., Khazendar, A., Larour, E., and Mouginot, J.: Dependence of century-scale projections of the Greenland ice sheet on its thermal regime, Journal of Glaciology, 59, 1024–1034, 2013.

Shi, Y. and Liu, S.: Estimation on the response of glaciers in China to the global warming in the 21st century, Chinese Science Bulletin, 45, 668–672, 2000.

Sugiyama, S., Sakakibara, D., Matsuno, S., Yamaguchi, S., Matoba, S., and Aoki, T.: Initial field observations on Qaanaaq ice cap, northwestern Greenland, Annals of Glaciology, 55, 25–33, 2014.

Sun, W., Qin, X., Ren, J., Yang, X., Zhang, T., Liu, Y., Cui, X., and Du, W.: The surface energy budget in the accumulation zone of the Laohugou Glacier No.12 in the western Qilian Mountains, China, in summer 2009, Arctic, Antarctic, and Alpine Research, 44, 296–305, 2012.

Svensson, H.: Is the cross-section of a glacial valley a parabola?, Journal of Glaciology, 3, 362–363, 1959.

Tian, H., Yang, T., and Liu, Q.: Climate change and glacier area shrinkage in the Qilian Mountains, China, from 1956 to 2010, Annals of Glaciology, 55, 187–197, 2014.

Van der Veen, C. J.: A numerical scheme for calculating stresses and strain rates in glaciers, Mathematical geology, 21, 363–377, 1989.

Vincent, C., Le Meur, E., Six, D., Possenti, P., Lefebvre, E., and Funk, M.: Climate warming revealed by englacial temperatures at Col du Dôme (4250 m, Mont Blanc area), Geophysical Research Letters, 34, L16 502, 2007.

Wang, Y., Ren, J., Qin, X., Liu, Y., Zhang, T., Chen, J., Li, Y., and Qin, D.: Ice depth and glacier-bed characteristics of Laohugou Glacier No.12, Qilian Mountains, revealed by ground-penetrating radar. (in Chinese with English summary), Journal of Glaciology and Geocryology, 1, 28–35, 2016.

Wilson, N. J. and Flowers, G. E.: Environmental controls on the thermal structure of alpine glaciers, The Cryosphere, 7, 167–182, 2013.

Wilson, N. J., Flowers, G. E., and Mingo, L.: Comparison of thermal structure and evolution between neighboring subarctic glaciers, Journal of Geophysical Research: Earth Surface, 118, 1443–1459, 2013.

Yao, T., Thompson, L., Yang, W., Yu, W., Gao, Y., Guo, X., Yang, X., Duan, K., Zhao, H., and Xu, B.: Different glacier status with atmospheric circulations in Tibetan Plateau and surroundings, Nature Climate Change, 2, 663–667, 2012.

Zhang, T., Xiao, C., Colgan, W., Qin, X., Du, W., Sun, W., Liu, Y., and Ding, M.: Observed and modelled ice temperature and velocity along the main flowline of East Rongbuk Glacier, Qomolangma (Mount Everest), Himalaya, Journal of Glaciology, 59, 438–448, 2013.

Zhang, T., Ju, L., Leng, W., Price, S., and Gunzburger, M.: Thermomechanically coupled modelling for land-terminating glaciers: a comparison of two-dimensional, first-order and three-dimensional, full-Stokes approaches, Journal of Glaciology, 61, 702–712, 2015.

Zwinger, T. and Moore, J.: Diagnostic and prognostic simulations with a full Stokes model accounting for superimposed ice of Midtre Lovénbreen, Svalbard, The Cryosphere, 3, 217–229, 2009.

Table 1. Parameters used in this study

Symbol	Description	Value	Unit
β	Clausius-Clapeyron constant	8.7×10^{-4}	K m^{-1}
g	Gravitational acceleration	9.81	m s^{-2}
ρ	Ice density	910	kg m^{-3}
ρ_{w}	Water density	1000	kg m^{-3}
n	Exponent in Glen's flow law	3	-
$\dot{\epsilon}_0$	viscosity regularization	10^{-30}	a^{-1}
A_0	Flow law parameter		
	when T ≤ 263.15 K	3.985×10^{-13}	Pa^{-3} s^{-1}
	when T > 263.15 K	1.916×10^{3}	Pa^{-3} s^{-1}
Q	Creep activation energy		
	when T ≤ 263.15 K	60	kJ mol^{-1}
	when T > 263.15 K	139	kJ mol^{-1}
R	Universal gas constant	8.31	J mol^{-1} K^{-1}
k	Thermal conductivity	2.1	W m^{-1} K^{-1}
c_p	Heat capacity of ice	2009	J kg^{-1} K^{-1}
L	Latent heat of fusion of ice	3.35×10^{-5}	J kg^{-1}
T_0	Triple-point temperature of water	273.16	K

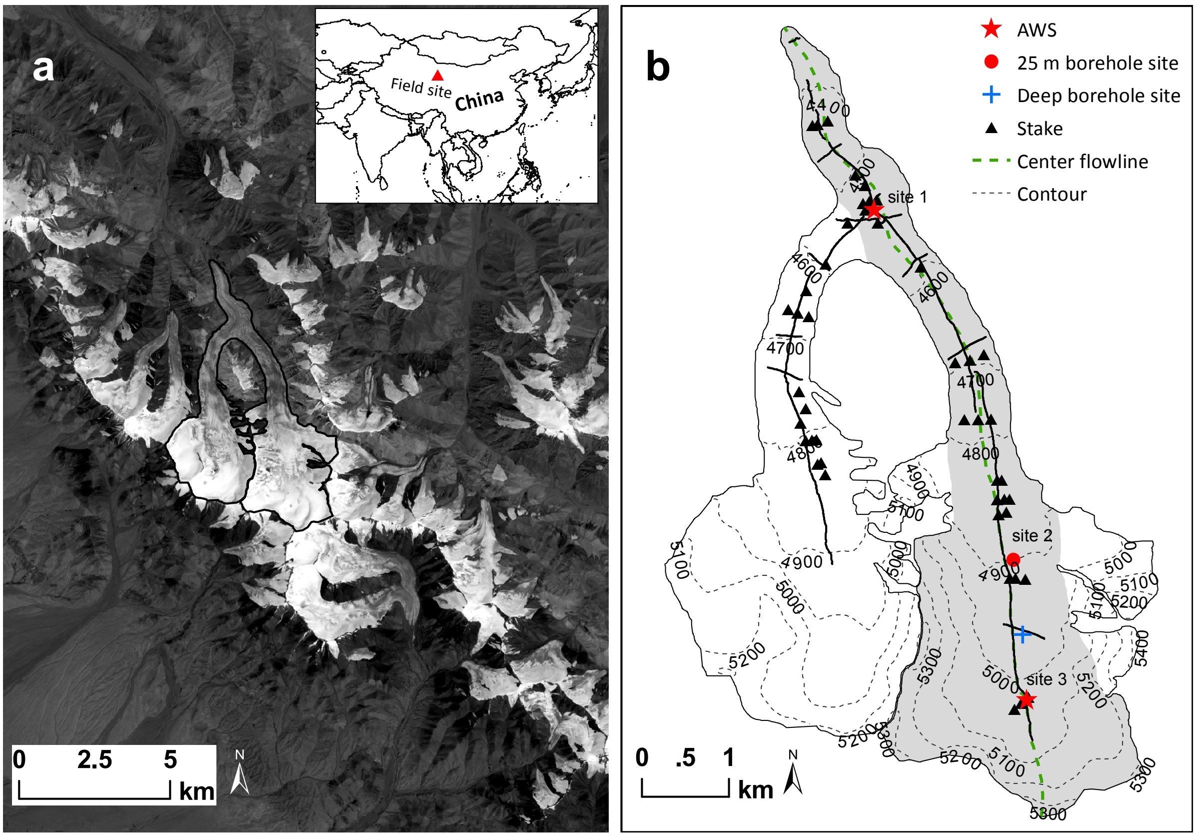

Figure 1. (a) The location of Laohugou Glacier No.12 (LHG12) in the west Mt. Qilian Shan, China. (b) The solid and thick black lines indicate the ground-penetrating radar (GPR) survey lines. The shaded area denotes the mainstream of LHG12, which only includes the east branch and neglects the west branch and all small tributaries. The green dashed line represents the center flowline. Red stars indicate the locations of the automatic weather stations (AWSs) and the 25 m deep shallow boreholes (sites 1 and 3). A solid red circle represents the location of the shallow borehole at site 2, and a blue cross represents the location of the deep ice borehole. Black triangles show the positions of the stakes used for ice surface velocity measurements. The black contours are generated from SRTM DEM in 2000.

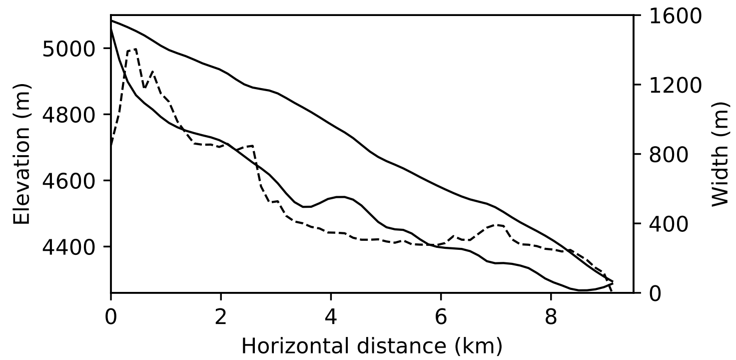

Figure 2. The glacier geometry of LHG12 along the center flowline. Solid lines show the glacier surface and bed elevations, while the dashed line shows the variation of glacier half widths along the flowline.

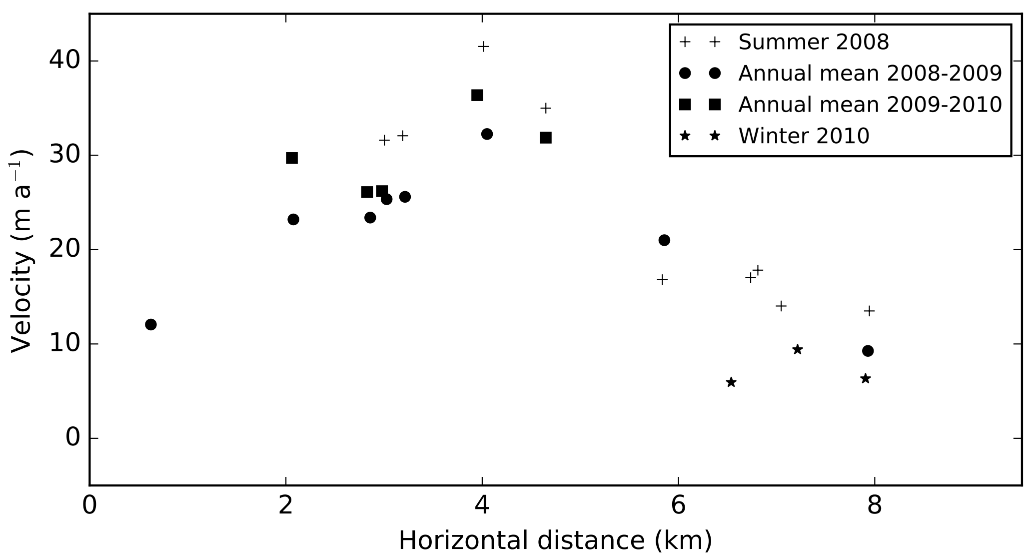

Figure 3. Measured ice surface velocities along the center flowline.

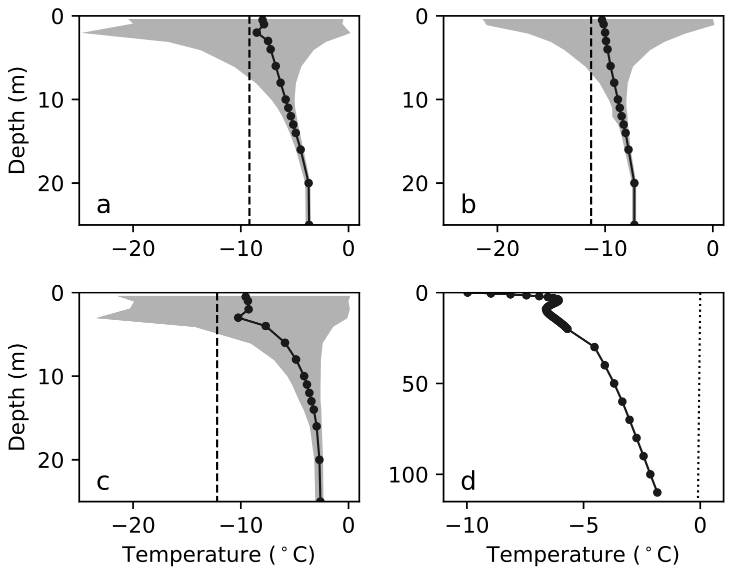

Figure 4. Ice temperature measurements from four ice boreholes. (a, b, c) Ice temperature measurements from the 25 m deep boreholes at site 1, 2, and 3, respectively. The black dots show the mean annual ice temperatures over the period of 2010 – 2011. The shaded areas show the yearly fluctuation range of the ice temperature. The dashed lines indicate the mean annual air temperature. (d) Measured ice temperatures from the deep borehole. The dotted line indicates the pressure-melting point (PMP) as a function of ice depth.

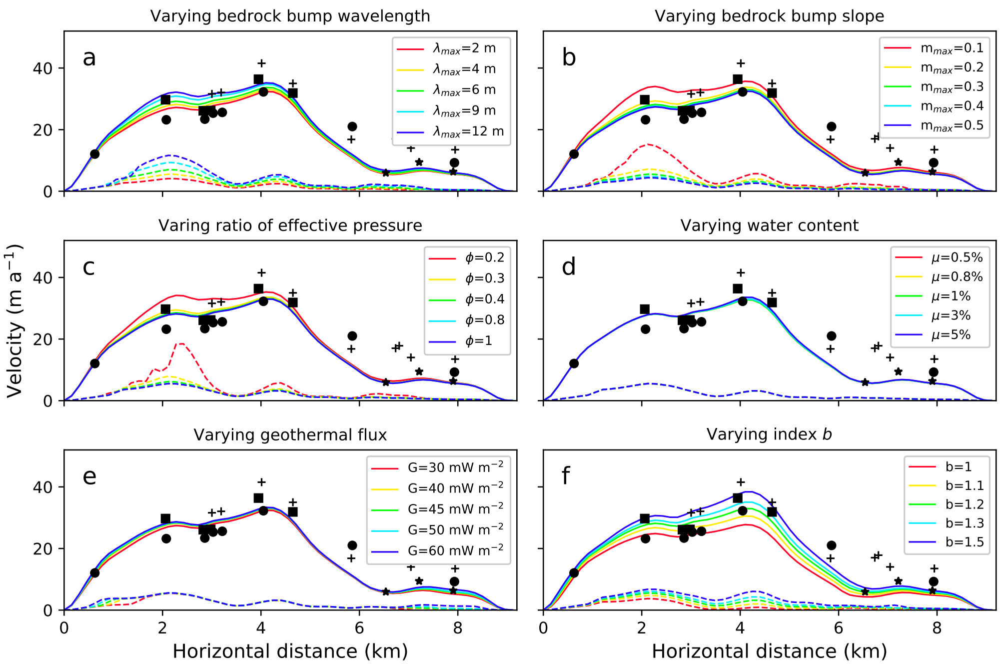

Figure 5. Sensitivity of modeled ice flow speeds to parameters along the CL. The solid and dashed lines indicate the modeled surface and basal sliding velocities, respectively. Symbols show the measured ice surface velocities (Fig. 3).

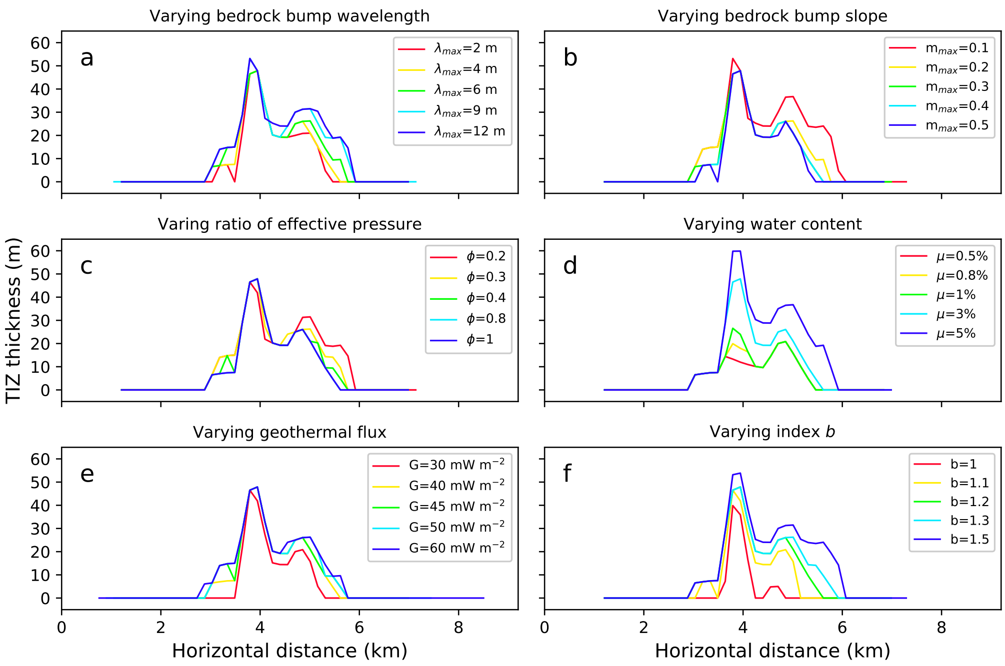

Figure 6. Sensitivity of modeled temperate ice thicknesses to parameters along the CL. The parameter settings are the same as described in Fig. 5.

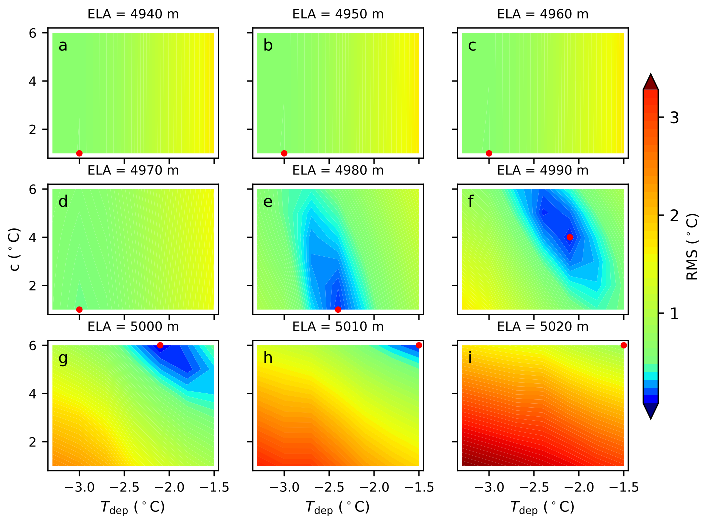

Figure 7. Root mean squares (RMS) of differences between measured and modeled temperature profiles in the deep borehole. The red circle indicates the minimum of RMS. The parameter T_{dep} is varied from $-3.3\,^{\circ}\text{C}$ to $-1.5\,^{\circ}\text{C}$ with a step-size of $0.3\,^{\circ}\text{C}$, while c is varied in the range of $1 - -6\,^{\circ}\text{C}$ with a step-size of $1\,^{\circ}\text{C}$. The equilibrium line altitude (ELA) is fixed in each panel.

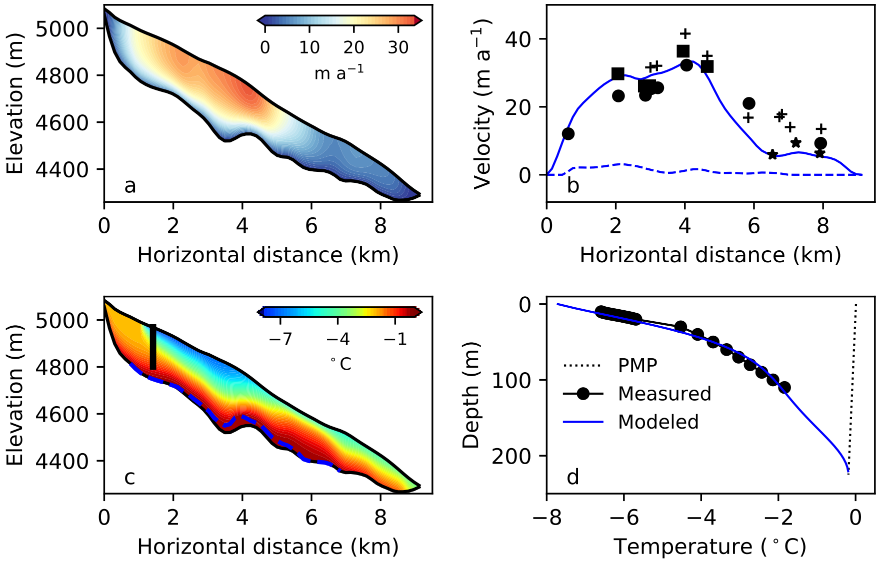

Figure 8. Comparison of measured and diagnostically modeled horizontal velocities and ice temperatures of LHG12. (a) Modeled distribution of horizontal ice velocity. (b) Measured (symbols) and modeled (solid line) surface and basal (dashed line) horizontal velocities. The symbols are measured surface ice velocities (see the manuscript). (c) Modeled distribution of ice temperature. The blue dashed line indicates the CTS position, and the black bar shows the location of the deep ice borehole. (d) Modeled (blue line) and measured (dots) ice temperature profiles for the deep borehole. Pressure-melting point is shown by the dotted line.

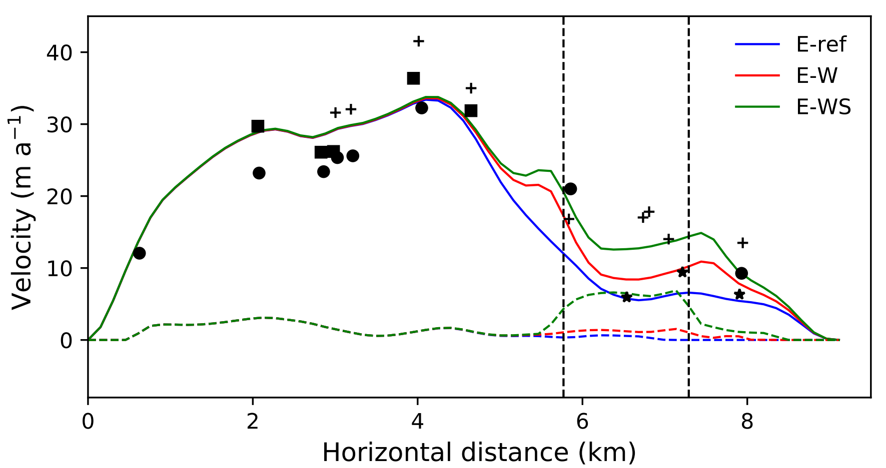

Figure 9. Modeled ice velocities for experiments E-ref (blue line), E-W (red line), and E-WS (green line). The glacier widths in the zone of km 5.8 – 7.3 (bounded by the vertical dashed lines) are increased by 450 m for E-W and E-WS. In E-WS we also include a basal sliding enhancement between km 5.8 – 7.3.

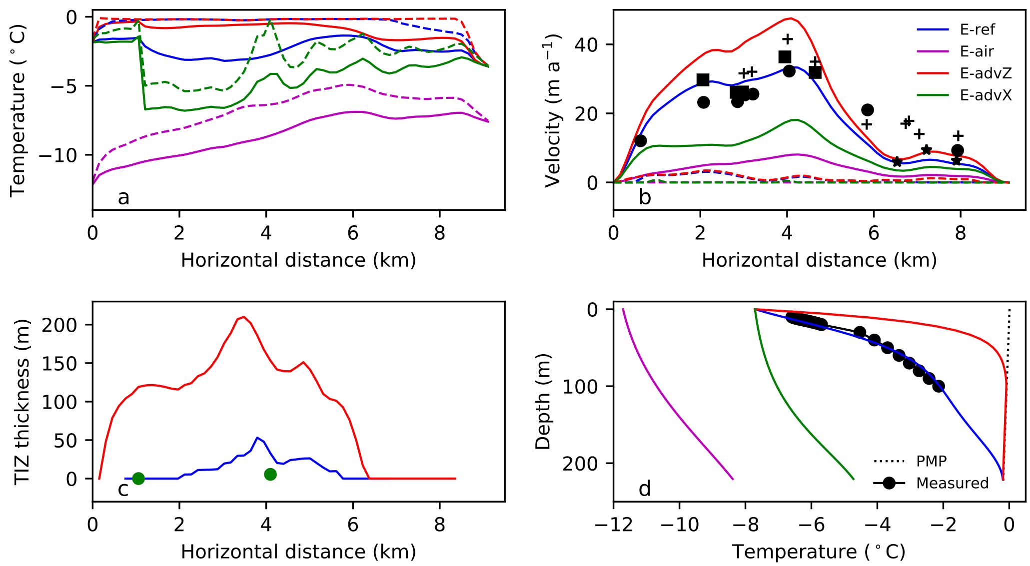

Figure 10. Modeled ice temperatures and velocities for experiments E-ref (blue line), E-air (pueple line), E-advZ (red line) and E-advX (green line). (a) Modeled column mean (solid lines) and basal (dashed lines) ice temperatures along the CL. (b) Modeled surface (solid lines) and basal (dashed lines) ice velocities along the CL. The symbols for the measured ice surface velocities are the same as those shown in Fig. 3. (c) Modeled TIZ thickness. (d) Measured (dots) and modeled (coloured lines) ice temperature profiles for the deep borehole. The dotted line shows the pressure-melting point as a function of ice depth.

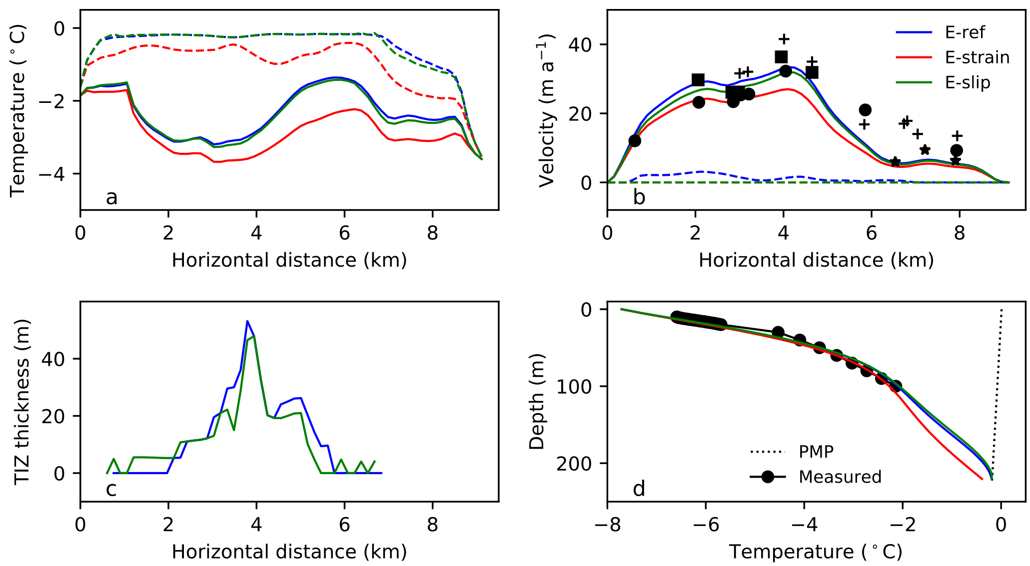

Figure 11. Modeled ice temperatures and velocities for experiments E-ref (blue line), E-strain (red line) and E-slip (green line). (a) Modeled column mean (solid lines) and basal (dashed lines) ice temperatures along the CL. (b) Modeled surface (solid lines) and basal (dashed lines) ice velocities along the CL. The symbols for the measured ice surface velocities are the same as those shown in Fig. 3. (c) Modeled TIZ thickness. (d) Measured (dots) and modeled (coloured lines) ice temperature profiles for the deep borehole. The dotted line shows the pressure-melting point as a function of ice depth.

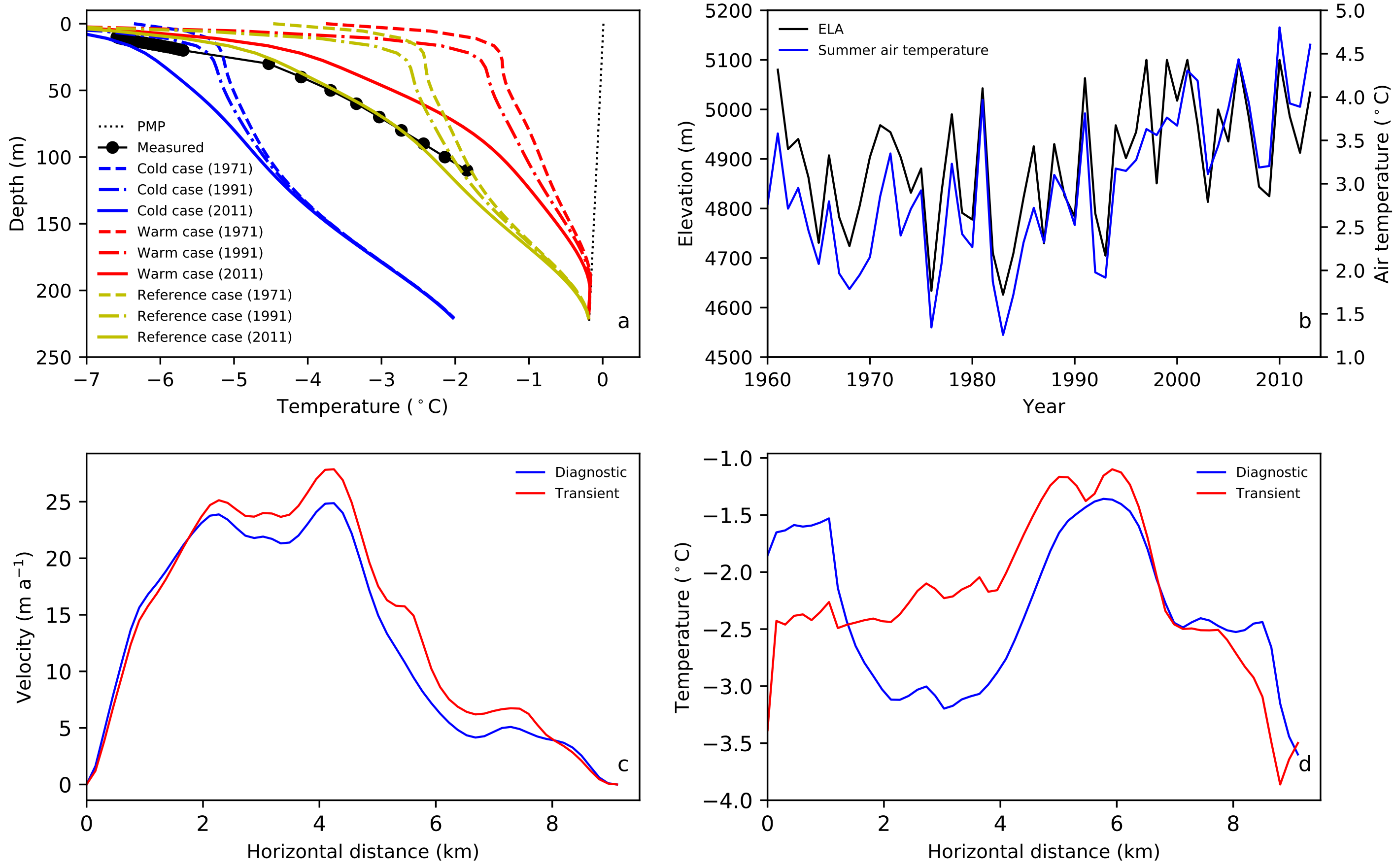

Figure 12. (a) Modeled temperature profiles in the deep borehole for $T_{\mathrm{dep}} = -5^{\circ}\mathrm{C}$ (cold case), $-2.1^{\circ}\mathrm{C}$ (reference case) and $-1^{\circ}\mathrm{C}$ (warm case). (b) The variations of ELA and summer air temperature at 4200 m a.s.l. during 1961–2011. (c) The vertically averaged ice velocity profiles along x for the diagnostic and transient simulation (reference case); (d) The vertically averaged ice temperature profiles along x for the diagnostic and transient simulation (reference case);